WO$_3$ nanoneedles/α-Fe$_2$O$_3$/cobalt phosphate composite photoanode for efficient photoelectrochemical water splitting

Tao Jin [a], Peng Diao [a,*], Qingyong Wu [a], Di Xu [a], Dianyi Hu [a], Yonghong Xie [a], Mei Zhang [b,*]

[a] Key Laboratory of Aerospace Materials and Performance (Ministry of Education), School of Materials Science and Engineering, Beihang University, Beijing 100191, PR China
[b] State Key Laboratory of Advanced Metallurgy, School of Metallurgical and Ecological Engineering, University of Science and Technology Beijing, Beijing 100083, PR China

ABSTRACT

We report the fabrication of the WO$_3$ nanoneedles/α-Fe$_2$O$_3$ heterojunction photoanodes for efficient photoelectrochemical water splitting. The high-aspect-ratio single crystalline WO$_3$ nanoneedles (NNs) act as both the photoanode framework and the light harvester in the UV and blue visible region. The porous layer of small α-Fe$_2$O$_3$ nanocrystals act as a cooperative light harvester in the visible region. The WO$_3$ NNs/α-Fe$_2$O$_3$ heterojunction photoanodes exhibit an extended light absorption band in the visible region and a significantly enhanced photocurrent density, which is ca. 1.6 times higher than that obtained on the pure WO$_3$ NNs. Cobalt phosphate (Co-Pi) was employed as an oxygen evolving catalyst to modify the heterojunction electrode, and the resulting WO$_3$ NNs/α-Fe$_2$O$_3$/Co-Pi composite photoanodes show an excellent photostability for oxygen evolution reaction.

© 2013 Elsevier B.V. All rights reserved.

1. Introduction

The direct conversion of solar energy to chemical fuels provides an attractive long-term solution to the problem of ever-rising global energy demand [1]. Solar powered water-splitting is an artificial photosynthesis that involves two half-cell reactions, the hydrogen evolution reaction (HER) and the oxygen evolution reaction (OER), and the solar energy is stored in the chemical bonds of the two products H$_2$ and O$_2$ [2]. The photoelectrochemical (PEC) cells are widely used as water splitting devices [2,3] because they spatially separate the two half-cell reactions, allowing the investigation of only one half-cell reaction. Of the two half-cell reactions, OER is more complex because it requires multiple bond rearrangements that involve the removal of four electrons and two protons from two H$_2$O molecules [4]. During the past decade, great efforts have been made to develop new photoanode catalysts to improve the solar-to-oxygen conversion efficiency.

The photoanodes for OER are usually composed of semiconductors whose valence band edge is more positive than the redox potential of O$_2$/H$_2$O couple [5]. Among various photoanode materials, WO$_3$ has attracted extensive attention [6–16] due to the highly positive position of its valence band edge (ca. 3.0 V vs NHE),

which provides large driving force for photogenerated holes to oxidize water. However, there are three main factors that prevent WO$_3$ from being a highly efficient and durable photoanode material for OER. First, WO$_3$ has a relatively large band gap of ca. 2.7 eV, which prevents WO$_3$ from absorbing the vast proportion of visible solar spectrum, thought it can capture approximately 12% of the solar spectrum in near-UV and visible blue regions [17]. Second, WO$_3$ is an indirect band-gap semiconductor, whose absorption coefficient is very low, especially for the photons with energies close to the band-gap [8,18], due to its short hole diffusion length of ca. 150 nm [8,19]. As a result, only when the holes are generated within the hole diffusion length from surface, can they contribute to the photo-driven water oxidation. Third, photocorrosion of WO$_3$ in neutral and basic solutions can greatly decrease its photoactivity [14].

In order to solve the first issue, semiconductors with band gap energies in the visible region of solar spectrum, such as Fe$_2$O$_3$, BiVO$_4$, and etc., were used to combine with WO$_3$ to form composite photoanodes whose absorption band covers the majority of the UV and visible portion of the solar spectrum. The improved efficiency obtained at the composite photoanodes, such as WO$_3$/Fe$_2$O$_3$ [20] and WO$_3$/BiVO$_4$ [21–23], confirmed the success of this strategy. As for the second issue, nanostructured WO$_3$ was used to prepare photoanodes to ensure that at least one dimension of the WO$_3$ nanostructures is smaller than the hole diffusion length (ca. 150 nm) so that all photogenerated holes can contribute to OER [7–9,11,24,25]. The smaller the nanoparticle size, the shorter the distance for the photogenerated hole to diffuse from inside WO$_3$ to

the WO_3/solution interface, and then the higher the PEC activity for OER [11,25]. However, photoanodes composed of small nanoparticles have large grain boundaries that may increase electron–hole recombination. Therefore, it is highly desirable to prepare WO_3 nanocrystals with high-aspect ratio in order to reduce grain boundaries while keeping the width smaller than hole diffusion length. To solve the third issue, an oxygen evolving catalyst was deposited on the surface of WO_3 to facilitate the transfer of photogenerated holes from WO_3 to water [14,26], and then suppressed the photocorrosion induced by hole accumulation at WO_3/electrolyte interface [14].

Herein, we report the fabrication of the WO_3 nanoneedles/α-Fe_2O_3/cobalt phosphate composite electrodes to enhance the photoactivity and stability of photoanode toward solar-powered OER. The single crystalline high-aspect ratio WO_3 nanoneedles (NNs) act as both the photoanode framework and the light harvester in the UV and blue visible region. The porous hematite layer composed of small α-Fe_2O_3 nanoparticles act as a cooperative light absorber in the visible region, and the cobalt phosphate (Co-Pi) [27] act as the electrochemical oxygen evolving catalyst. The key advantages of the composite photoanode are as follows. (1) It has a light absorption band broadened to 650 nm. (2) The single crystalline WO_3 NNs framework greatly inhibits electron–hole recombination due to the inherently good electron transport properties of WO_3 [28]. (3) The NNs framework provides an ultra-large specific interfacial areas between semiconductors and solution, where photoinduced holes oxidize water to generate O_2. We demonstrate in this work that the composite photoanodes exhibit greatly improved photoactivity and stability for OER.

2. Experimental

2.1. Preparation of WO_3 NNs

WO_3 NNs were prepared on fluorine-doped tin oxide (FTO) substrates ($8\,\Omega\,sq^{-1}$, transparency 80%, Asahi Glass, Japan) by a two-step hydrothermal method that was a modification of the previously reported approach [9]. The first step is a nanoseed-generating step in which the FTO substrates were immersed in aqueous solution prepared by dissolving 0.313 g of H_2WO_4 and 0.125 g of poly(vinyl alcohol) in 10 mL H_2O. Then hydrothermal reaction was carried out at 250 °C for 2 h. The second step, which allowed for the growth of nanoseeds to form WO_3 NNs, was accomplished by immersing the nanoseed-modified FTO substrates in the mixture of 3 mL of 0.05 M H_2WO_4, 0.2 g of oxalic acid, 0.5 mL of 6 M HCl, and 10 mL of acetonitrile, and raising the temperature of the mixture in an autoclave to 180 °C for 2 h.

2.2. Deposition of Fe_2O_3 layer on WO_3 NNs

The Fe_2O_3 layer was prepared by firstly growing FeOOH on the surface of WO_3 NNs, and then transforming FeOOH to α-Fe_2O_3 by annealing. FeOOH was grown on WO_3 NNs by a hydrothermal method [29], in which the WO_3 NNs modified FTO substrates were immersed in aqueous solution containing 0.5 mM $FeCl_3$·$6H_2O$ and 0.5 mM urea. After 5 h of hydrothermal reaction at 100 °C in an autoclave, the substrates were annealed at 550 °C for 3 h.

2.3. Deposition of Co-Pi on the WO_3 NNs/Fe_2O_3 composite

The Co-Pi layer was deposited on the surface of WO_3 NNs/Fe_2O_3 composite using a photo-assisted electrodeposition method [30,31]. In detail, the WO_3 NNs/Fe_2O_3 composite electrodes were immersed in 0.1 M KH_2PO_4/K_2HPO_4 buffer solution (pH = 7) containing 0.5 mM $CoCl_2$, and then a deposition potential of 1.0 V

vs SCE was applied to the electrode for 900 s under xenon lamp illumination (120 mW cm^{-2}).

2.4. Photoelectrochemical measurements

All photoelectrochemical measurements were carried out on a CHI660A work station (CH Instruments Co.), using a 500 W xenon lamp as the light source. The maximum incident light intensity on the electrode surface was 120 mW cm^{-2}. The electrochemical measurements were performed in 0.1 M KH_2PO_4/K_2HPO_4 buffer solution (pH = 7), using Pt foil and SCE as counter and reference electrodes, respectively.

The incident photon-to-current conversion efficiency (IPCE) of different photoelectrodes was measured in a 0.1 M KH_2PO_4/K_2HPO_4 buffer solution (pH = 7) at 1.65 V vs RHE (1.0 V vs SCE) using a photoelectrochemical system comprising a monochromator (WDG15-Z), a 300 W xenon arc lamp, a light power meter, and a CHI660A work station.

3. Results and discussion

Fig. 1a shows a typical SEM image of the WO_3 NNs prepared on an FTO substrate. It can be clearly seen that the WO_3 NNs uniformly grew on FTO substrates with one ends protruding from the substrate. TEM images show that the NNs have a high-aspect ratio of ca. 15–70. Fig. 1b shows a typical high resolution TEM (HRTEM) image of an individual WO_3 NN. The distance between two adjacent lattice planes that are perpendicular to the long axis is 0.375 nm. This value matches well with the lattice spacing of the (0 2 0) planes of monoclinic WO_3, indicating a single crystalline structure with (0 2 0) orientation. The selected area electron diffraction (SAED) measurement was carried out to characterize crystal structure of the WO_3 NNs, and the result is shown in Fig. S1a in the supplementary material. The SAED pattern further confirms that the annealed WO_3 NNs have a single crystalline monoclinic structure. XRD was used to provide more information about the crystal structure of WO_3 NNs, and the result is presented in Fig. 2. The XRD pattern of the WO_3 NNs agrees well with that of monoclinic WO_3 (JCPDS: #83-951), and the high intensity of (0 2 0) peak indicates that the WO_3 NNs are (0 2 0)-oriented. These XRD results are in good agreement with the result of HRTEM (Fig. 1b) and SAED (Fig. S1a).

To modify the WO_3 NN framework with Fe_2O_3 nanoparticles, FeOOH was first grown on the surface of NNs by a hydrothermal method in the mixed solution of 0.5 mM $FeCl_3$ and 0.5 mM urea at 100 °C for 5 h [29]. Then, the resulting yellow WO_3 NNs/FeOOH composite was annealed at 550 °C for 3 h to generate the WO_3 NNs/Fe_2O_3 heterojunction photoanode. After annealing, the color of the film changed to red, suggesting successful conversion from FeOOH to hematite. Fig. 1c shows a typical SEM image of the Fe_2O_3 nanoparticle modified WO_3 NNs. After Fe_2O_3 modification, the NNs turned to square nanorods with a greatly increased average diameter of ca. 250 nm. The square nanorod morphology is due to the formation of orthorhombic FeOOH nanorods on WO_3 NNs during hydrothermal growth. After annealing, the square nanorod morphology was retained though the FeOOH crystals were transformed into Fe_2O_3 [29] (see Fig. S2, Fig. S3 and Fig. S4 in supporting information). Fig. 1d shows a typical HRTEM image of the WO_3 NNs/Fe_2O_3 square nanorods after annealing, from which the background lattice fringes of monoclinic WO_3 and a porous coating layer of small nanocrystals are clearly seen. The lattice spacing of the coating nanocrystals is 0.251 nm, which matches well with the value of the (1 1 0) plane of α-Fe_2O_3 [32,33], indicating that the porous coating layer consists of single crystalline α-Fe_2O_3 nanoparticles. The SAED pattern of the porous Fe_2O_3 nanorods prepared by annealing of the FeOOH nanorods is shown in Fig. S1b in the supplementary material. The well aligned diffraction pattern confirms that
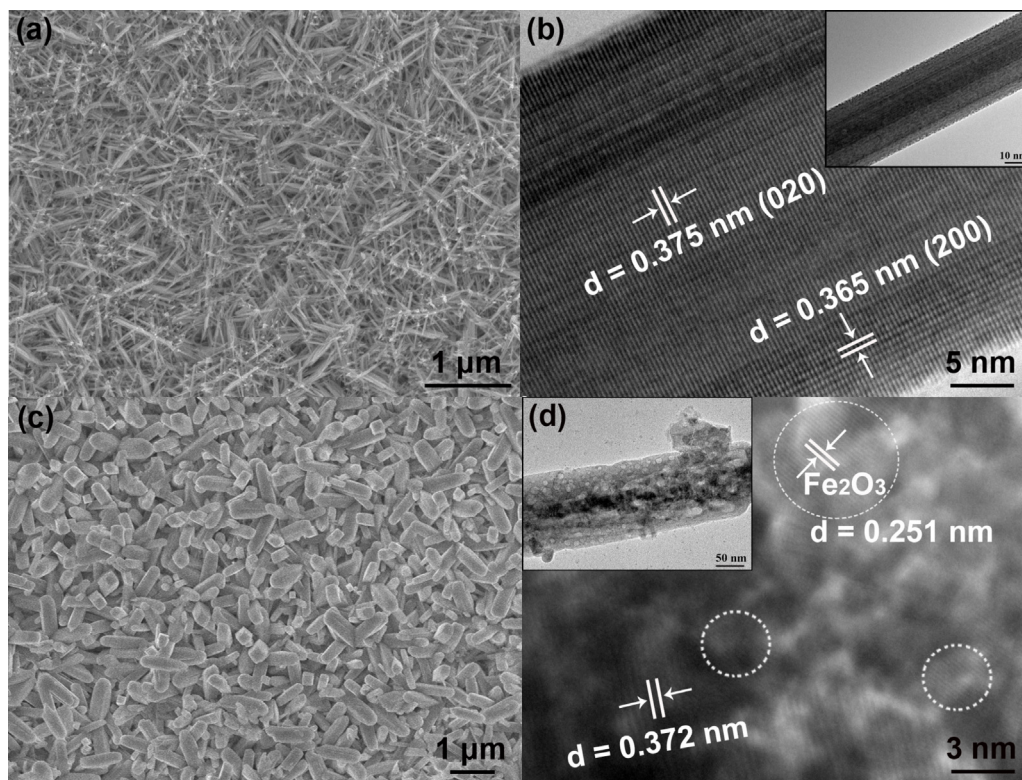
Fig. 1. SEM (a) and HRTEM (b) images of the WO₃ NNs. SEM (c) and HRTEM (d) images of the WO₃ NNs/Fe₂O₃ composite.

the obtained α-Fe_2O_3 exhibits a single crystalline structure. The porous structure of the Fe_2O_3 coating layer is attributed to the loss of water molecules in the FeOOH lattice and the formation of α-Fe_2O_3 nanocrystals during annealing [34]. The size distribution of α-Fe_2O_3 nanocrystals is in the range of 2–10 nm. On the basis of the HRTEM, XRD and SAED results, it can be safely concluded that the square nanorods shown in Fig. 1c are composed of the single crystalline WO₃ NN cores and porous shells made of α-Fe_2O_3 nanocrystals.

Fig. 2 shows the XRD patterns of the WO₃ NNs, the Fe_2O_3 nanoparticles, and the WO₃ NNs/Fe_2O_3 composite prepared on FTO substrates. After the WO₃ NNs were modified with Fe_2O_3 nanoparticles, a new diffraction peak appears at $2\theta = 35.9°$, which

corresponds to the (1 1 0) plane of α-Fe_2O_3 (JCPDS: #73-603) [29], indicating that the Fe_2O_3 nanocrystals have a preferential (110) orientation. This is consistent with the HRTEM observations of Fe_2O_3 nanocrystals shown in Fig. 1d, further confirming the successful preparation of the WO₃ NNs/Fe_2O_3 composite photoanode.

The light absorption is one of the most important properties of the photoanode materials for high efficient OER. Fig. 3 shows the UV–vis diffuse reflection spectra of the WO₃ NNs before and after the modification of the Fe_2O_3 nanocrystals. The pure WO₃ NNs have an absorption edge at ca. 450 nm, which is in agreement with the band gap energy of 2.7 eV and the previous results [6]. After deposition of the α-Fe_2O_3 nanocrystals on the WO₃ NNs, the absorption

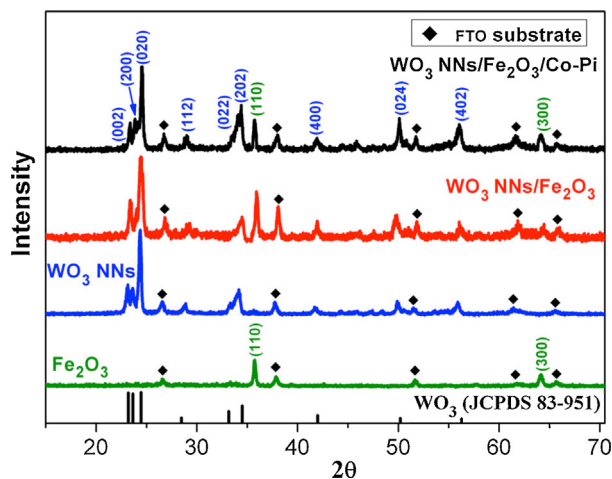**Fig. 2.** XRD patterns of the WO₃ NNs, the α-Fe_2O_3, the WO₃ NNs/Fe_2O_3 and the WO₃ NNs/Fe_2O_3/Co-Pi composites.
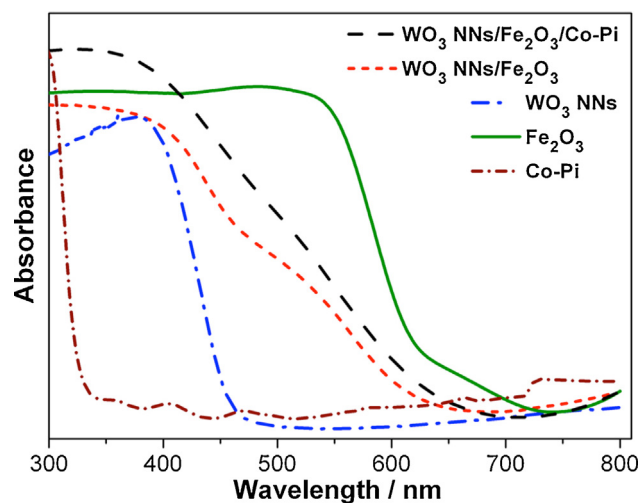

Fig. 3. UV–vis diffuse reflectance spectra of the WO₃ NNs, the α-Fe_2O_3, the WO₃ NNs/Fe_2O_3 composite, the Co-Pi film, and the WO₃ NNs/Fe_2O_3/Co-Pi composite.

edge of the WO_3 NNs/Fe_2O_3 composite photoanode was drastically extended to around 650 nm. The band gap energy of α-Fe_2O_3 nanocrystals, which was obtained from UV-vis spectrum based on Tauc equation, is 2.2 eV (Fig. S5 in supplementary material). The small band gap energy of α-Fe_2O_3 ensures that more light can be used to generate holes on the composite photoanodes.

The PEC water oxidation performances of the photoanodes were investigated using a three electrode system in 0.1 M KH_2PO_4/K_2HPO_4 buffer solution (pH = 7.0) under 120 mW cm^{-2} illumination. Fig. 4a shows the linear potential sweep voltammograms of the WO_3 NNs and the WO_3 NNs/Fe_2O_3 composite photoanodes in the dark and under illumination. Nearly no oxidation current can be observed within the entire potential sweep range without illumination, indicating that both the WO_3 NNs and the composite electrodes are inactive toward OER in the dark. However, under illumination, the WO_3 NNs electrode exhibits a large oxidation photocurrent that was ascribed to the oxidation of water [9,11,14,21,22]. The oxidation photocurrent starts to appear at ca. 0.59 V vs RHE. Moreover, a saturated photocurrent density starting from ca. 1.25 V vs RHE is obtained to be ca. 1.3 mA cm^{-2}. Both the low photocurrent onset potential and the high saturated photocurrent density indicate that the WO_3 NNs are highly active toward OER under illumination. We believe this is due to the following factors: (1) The diffusion distance of holes from where they are generated within WO_3 to the WO_3/solution interface is greatly decreased due to unique quasi one-dimension structure of WO_3 NNs. (2) The photoinduced electrons transfer efficiently through the NNs to the FTO substrate, leading to a great decrease of the electron–hole recombination. (3) The WO_3 NNs provide a large WO_3/solution interface where OER occurs.

After modification of the WO_3 NNs with α-Fe_2O_3, the resulting WO_3 NNs/Fe_2O_3 heterojunction photoanode exhibits a significantly improved activity toward OER under illumination. As shown in Fig. 4a, the saturated photocurrent density is increased to ca. 2.1 mA cm^{-2}, which is about 1.6 times higher than that of the pure WO_3 NNs. As mentioned above, the light absorption band extends greatly after Fe_2O_3 decoration, which means that more visible spectrum can be absorbed by the composite photoanode. In detail, the visible spectrum from 450 nm to 650 nm, which can not be absorbed by WO_3, can now be used to generate electron–hole pairs by α-Fe_2O_3 nanocrystals. As a result, more photo-induced holes contribute to the oxidation current under illumination. In addition, the small size of α-Fe_2O_3 nanocrystals may further improve the PEC efficiency of OER by not only decreasing the hole diffusion distance but also increasing the Fe_2O_3/solution interfacial area.

To further investigate the PEC performance of the WO_3 NNs and the WO_3 NNs/Fe_2O_3 composite photoanodes, current-potential curves were recorded under chopped irradiation, as shown in Fig. 4b. Both photoanodes exhibit nimble photo-response in nearly the whole potential sweep range, demonstrating the photo-generated holes are efficiently separated and transferred to the photoanode/solution interfaces, and then contribute to water oxidation. The saturated photocurrents of the WO_3 NNs and the WO_3 NNs/Fe_2O_3 composite photoanodes are 1.2 mA cm^{-2} and 1.9 mA cm^{-2}, respectively. The saturated photocurrent of the composite photoanode is also 1.6 times greater than that of the pure WO_3 NNs, which is in excellent agreement with the result under continuous irradiation.

The photocurrent onset potential can be obtained more accurately in Fig. 4b because both the photocurrent and the dark current
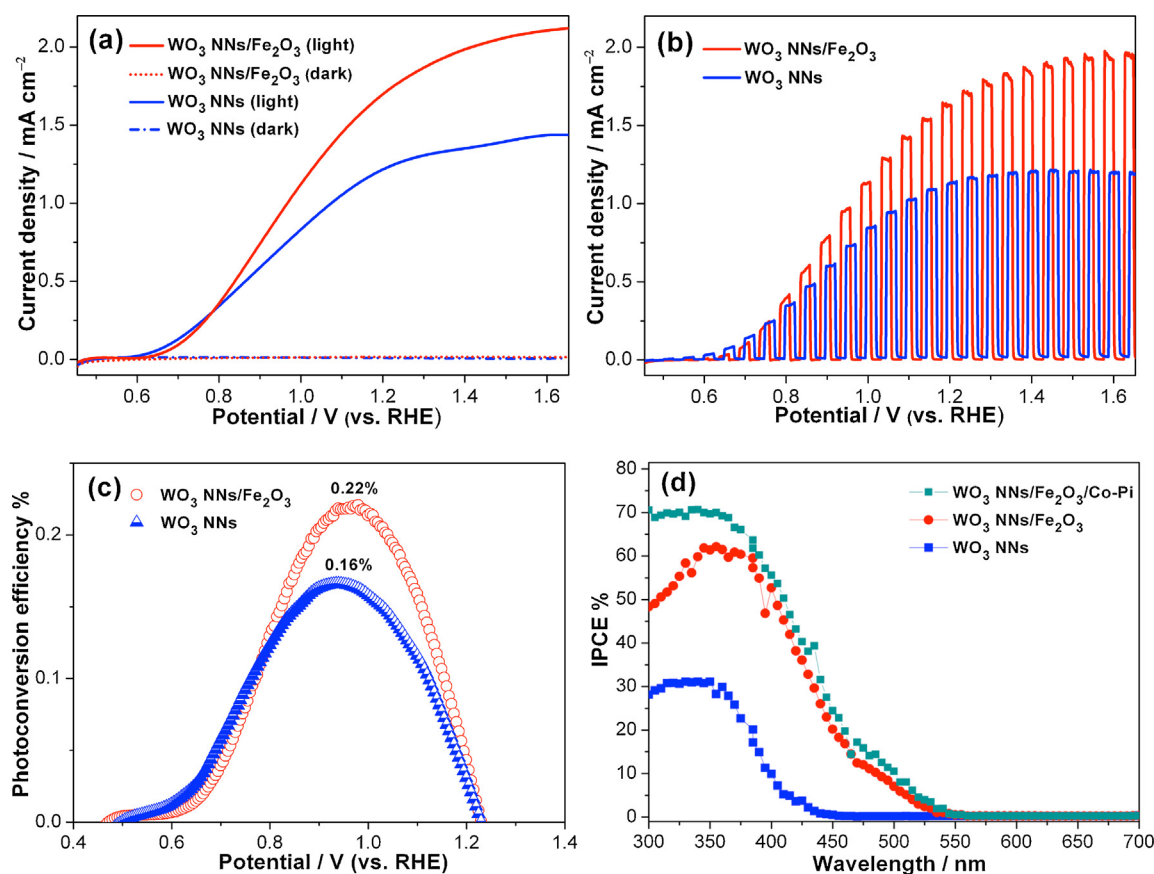

Fig. 4. Current–potential responses of the WO_3 NNs and the WO_3 NNs/Fe_2O_3 composite photoanodes in 0.1 M KH_2PO_4/K_2HPO_4 buffer solution (pH = 7) in the dark and under illumination (a) and under chopped illumination (b). (c) Applied bias photo-to-current efficiency as a function of applied potential for the WO_3 NNs and the WO_3 NNs/Fe_2O_3 composite photoanodes. (d) IPCE spectra of the WO_3 NNs, the WO_3 NNs/Fe_2O_3 composite and the WO_3 NNs/Fe_2O_3/Co-Pi composite photoanodes at 1.65 V vs RHE.

are involved in one current-potential curve under chopped illumination. Fig. 4b clearly shows that the photocurrent onset potential of both photoanodes is ca. 0.55 V vs RHE, which is negatively shifted by approximately 0.10 V compared to that reported previously in the exactly the same solution [14].

The photocurrent density shown in Fig. 4a can be used to calculate the applied bias photo-to-current efficiency (η) according to the following equation [35,36]

$$\eta = j_p \times \frac{(1.23 - |V|)}{I_0} \tag{1}$$

where j_p is the photocurrent density (mA cm^{-2}), V is the applied potential vs RHE (V), and I_0 is the incident light power density (mW cm^{-2}). Fig. 4c shows the variation of η as a function of the applied potential. The WO$_3$ NNs photoanode exhibits a maximum efficiency of 0.16% at 0.95 V vs RHE. After Fe$_2$O$_3$ modification, the maximum efficiency of the resulting WO$_3$ NNs/Fe$_2$O$_3$ heterojunction photoanode is increased to 0.22%, which represents a 1.4-fold improvement compared to the WO$_3$ NNs, indicating that the α-Fe$_2$O$_3$ nanocrystals greatly improve the utilization of solar spectrum. Moreover, the photoconversion efficiency of the composite photoanode is as high as, or higher than the η values recently obtained on other photoanodes, such as the reduced graphene oxide/WO$_3$ composite [16], the nitrogen-doped ZnO nanowire [37].

In order to investigate the quantitative correlation of light absorption on the WO$_3$ NNs and the WO$_3$ NNs/Fe$_2$O$_3$ composite photoanodes, IPCE measurements were carried out under illumination at 1.65 V vs RHE (corresponding to 1.00 V vs SCE). The potential of 1.65 V vs RHE was applied to the photoanode because a saturated photocurrent was obtained at this potential bias. The IPCE was calculated based on the equation [35,36]

$$IPCE = \frac{(1240 \times j_p)}{(\lambda \times I_0)} \tag{2}$$

where j_p is the photocurrent density (mA cm^{-2}), λ is the incident light wavelength, and I_0 is the incident light power density (mW cm^{-2}). As shown in Fig. 4d, the WO$_3$ NNs photoanode exhibited a maximum IPCE value of 31% at 350 nm. While the WO$_3$ NNs/Fe$_2$O$_3$ composite photoanode showed a much higher IPCE value in the wavelength range from 570 nm to 300 nm, with a maximum IPCE value of ca. 60%, suggesting that more light can be absorbed by the composite photoanode and used to generate hole to oxidize water. This result provides solid evidence that the combination of α-Fe$_2$O$_3$ with WO$_3$ NNs greatly improved photo-to-oxygen efficiency by benefiting the light absorption and the charge separation processes.

The deposition amount of α-Fe$_2$O$_3$ may influence the PEC oxygen-evolving performance of the WO$_3$ NNs/Fe$_2$O$_3$ composite photoanode. To study this issue, the deposition amount was controlled by varying the hydrothermal growth time of FeOOH on WO$_3$ NNs before annealing to form α-Fe$_2$O$_3$. Typical SEM images and the corresponding cross-section diameter distribution of the WO$_3$ NNs/Fe$_2$O$_3$ composite nanorods prepared with different FeOOH growth time were shown in Fig. S6 in the supplementary material. In order to clearly show the increase of the Fe$_2$O$_3$ shell thickness with increasing FeOOH growth time, we made a statistic analysis of the cross section diameter of the WO$_3$ NNs/Fe$_2$O$_3$ composite nanorods on the basis of SEM images. The time-dependent diameter distribution of the composite nanorods clearly demonstrates that the thickness of Fe$_2$O$_3$ layer increases with increasing FeOOH growth time (Fig. S6c). Because the diameter of the core WO$_3$ NNs does not change, the diameter increase of the composite nanorods reflects the increase of the Fe$_2$O$_3$ shell thickness. Therefore, the thickness of Fe$_2$O$_3$ layer with FeOOH growth time of 5 h is calculated to be about 100 nm.
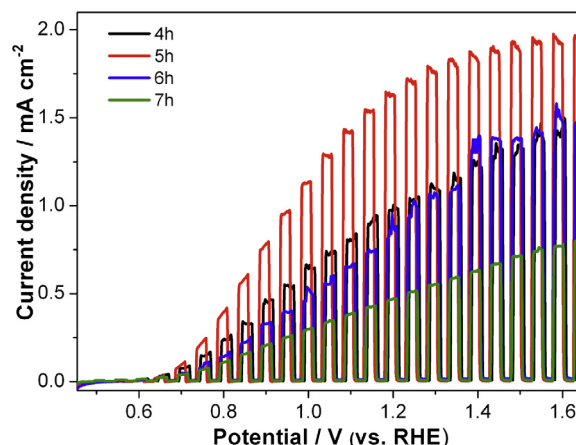

Fig. 5. Current–potential responses of the WO$_3$ NNs/Fe$_2$O$_3$ composite photoanodes prepared by hydrothermal growth of FeOOH on WO$_3$ NNs for different time and then annealing at 550 °C for 3 h. The current–potential curves were recorded in 0.1 M KH$_2$PO$_4$/K$_2$HPO$_4$ buffer solution (pH = 7) under chopped illumination.

The PEC oxygen-evolving performance of the WO$_3$ NNs/Fe$_2$O$_3$ composite photoanode was investigated as a function of the FeOOH growth time. Fig. 5 shows the current-potential responses of the composite photoanodes prepared with different FeOOH growth time. The photocurrent firstly increases with increasing hydrothermal growth time and reaches its maximum value at 5 h. When the growth time exceeds 5 h, the photocurrent decreases significantly. As shown in Fig. 5, the photocurrents obtained at 1.15 V vs RHE on the photoanodes with 6 and 7 h growth time were only 50% and 29% of the value obtained on the sample with 5 h growth time, respectively. We believe the dependence of photoactivity on the growth time is due to the following two opposite effects. On the one hand, shorter growth time results in thinner α-Fe$_2$O$_3$ layer, and then leads to insufficient utilization of visible band (450–650 nm) of solar spectrum by hematite. While on the other hand, longer growth time results in thicker α-Fe$_2$O$_3$ layer, which inevitably reflects more UV and blue visible light, and then leads to less absorption by the inner WO$_3$ NNs. Moreover, thicker α-Fe$_2$O$_3$ layer not only results in larger ohmic resistance but also introduces more grain boundaries and interfaces, which can act as electron–hole recombination centers and then greatly reduce the efficiency of the overall charge separation [38]. Therefore, we believe the maximum photocurrent observed in Fig. 5 is the result of a balance between the above-mentioned two opposite effects.

The photocatalytic stability is crucial for the long-term application of the WO$_3$ NNs/Fe$_2$O$_3$ composite in PEC water splitting. Fig. 6 shows the variation of photocurrents as a function of time at different constant applied potentials in 0.1 M KH$_2$PO$_4$/K$_2$HPO$_4$ buffer solution under chopped illumination. The fluctuation of the photocurrent observed in all curves is due to the disturbance of the photocurrent by forming and releasing O$_2$ bubbles. As shown in Fig. 6a, the photocurrents exhibit no discernable decay on both the WO$_3$ NNs and the composite photoanodes at the applied potential of 0.85 V vs RHE, indicating good stability at low overpotentials. However, after 1 h chopped illumination at potential of 1.15 V vs RHE, the photocurrents decline from 0.65 mA cm^{-2} to 0.42 mA cm^{-2} on the WO$_3$ NNs photoanode and from 1.30 mA cm^{-2} to 0.85 mA cm^{-2} on the composite photoanode, both showing a decay to 65% of their original values. These results suggest a faster decay at larger overpotentials. The decline of photocurrent is due to photocorrosion of WO$_3$ [14]. As was reported previously, photoinduced holes can generate tungsten peroxo species at the WO$_3$/solution interface, resulting in the photo-dissolution of
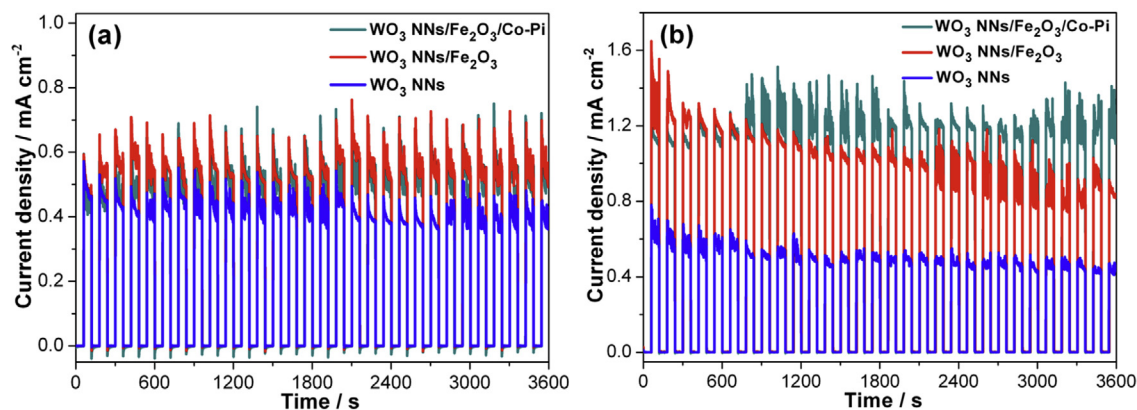
Fig. 6. Variation of photocurrent densities as a function of time at different constant bias of (a) 0.85 V and (b) 1.15 V vs RHE in 0.1 M KH_2PO_4/K_2HPO_4 buffer solution (pH = 7) under chopped illumination.

WO$_3$ [14]. This reaction is a competing reaction with OER [10,14]. Therefore, the factors that accelerate the accumulation of holes on the surface of WO$_3$ will aggravate the photocorrosion and then speed up the loss of photoactivity. Higher applied potentials induce stronger driving force for photogenerated holes to move toward WO$_3$/solution interface, and therefore lead to a faster accumulation rate of holes on WO$_3$ surface, which inevitably results in a faster decay of the photoactivity.

In order to improve the photostability of photoanodes, a strategy was proposed in which an oxygen-evolving catalyst, such as cobalt phosphate (Co-Pi) [27], was deposited on the photoanode to improve the kinetics of OER [14,30,31,39–41] and then to suppress the photocorrosion [14]. This strategy has been confirmed to be effective on WO$_3$ [14], Fe$_2$O$_3$ [30,39,40], ZnO [31], and BiVO$_4$ [41] photoanodes. In this work, we deposited Co-Pi on the WO$_3$ NNs/Fe$_2$O$_3$ composite using a photo-assisted electrodeposition method [30,31]. The resulting composite, which was referred as the WO$_3$ NNs/Fe$_2$O$_3$/Co-Pi photoanode, exhibits cyclic voltammetric features of the Co-Pi layer in the dark (Fig. S7), confirming the successful deposition of Co-Pi on the WO$_3$ NNs/Fe$_2$O$_3$ composite. The XRD spectrum of the WO$_3$ NNs/Fe$_2$O$_3$/Co-Pi composite is shown in Fig. 2. After Co-Pi modification, the resulting composite photoanode exhibits the same XRD pattern as that of the WO$_3$ NNs/Fe$_2$O$_3$ composite. This result is in good agreement with the amorphous nature of Co-Pi layer [27]. The UV–vis spectra of the pure Co-Pi film and the WO$_3$ NNs/Fe$_2$O$_3$/Co-Pi composite are presented in Fig. 3. The pure Co-Pi film has a very low absorption in the wavelength range from 320 nm to 800 nm. The low light absorption endows Co-Pi layer with high optical transparency, which is very important for efficient OER using Co-Pi as an oxygen evolving catalyst to couple with light-harvesting semiconductors. After deposition of Co-Pi, the resulting WO$_3$ NNs/Fe$_2$O$_3$/Co-Pi composite exhibits absorption features similar to those of the WO$_3$ NNs/Fe$_2$O$_3$ composite, providing further evidence that the Co-Pi modification has little effect on the light-harvesting performance of the semiconductor photoanode. A typical HRTEM image of the WO$_3$ NNs/Fe$_2$O$_3$/Co-Pi composite is shown in Fig. S8 in the supplementary material. Because the Co-Pi tends to deposit at the photoactive sites on WO$_3$ surface during photo-assisted electrodeposition [31], the obtained Co-Pi layer is not uniform and does not completely coat the surface of WO$_3$ NNs. The thickness of the Co-Pi layer prepared in this work varies from about less than 1 nm to over 3 nm, as can be seen in Fig. S8.

Similar to the WO$_3$ NNs/Fe$_2$O$_3$ electrode, the WO$_3$ NNs/Fe$_2$O$_3$/Co-Pi composite photoanode shows high activity toward OER under illumination (see Fig. S9 in supporting information). The IPCE of the WO$_3$ NNs/Fe$_2$O$_3$/Co-Pi composite photoanode
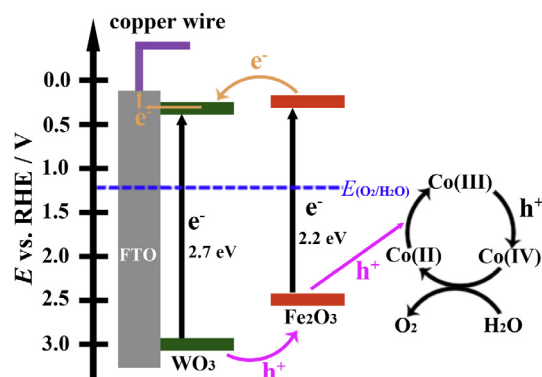

Fig. 7. Schematic of the band diagram of the WO$_3$ NNs/Fe$_2$O$_3$/Co-Pi composite photoanode for photoelectrochemical OER.

also increases compared to that of the composite photoanode without the Co-Pi layer, as shown in Fig. 4d. More importantly, after deposition of Co-Pi, the photoanode exhibits no discernable decay in photocurrent density even at potential of 1.15 V vs RHE (see Fig. 6b), indicating an excellent photostability. We believe that, as an oxygen evolving catalyst, Co-Pi can efficiently mediates the transfer of photogenerated holes from semiconductor to water. Therefore, the presence of Co-Pi on the surface of photoanode effectively prevents the photocorrosion of WO$_3$ and Fe$_2$O$_3$ by suppressing hole accumulation on the semiconductor/solution interface, and then improves the photostability of the electrode.

Fig. 7 illustrates the solar-driven OER mechanism on the WO$_3$ NNs/Fe$_2$O$_3$/Co-Pi photoanode. The valence band edges of WO$_3$ and Fe$_2$O$_3$ are located at ca. 3.0 V and 2.5 V vs NHE, respectively. Under irradiation, photoinduced holes are spontaneously injected from the valence band of WO$_3$ into that of Fe$_2$O$_3$. This implies that, after Fe$_2$O$_3$ decoration, more photo-induced holes are not only generated within the composite photoanode but also transferred to the electrode/solution interfaces and contribute to OER. Applying positive potential to the photoanode not only facilitates the hole injection process but also accelerates the hole diffusion to the photoanode/solution interface, where the holes oxidize water. As for the photoinduced electrons, they are spontaneously injected from the conduction band of Fe$_2$O$_3$ into that of WO$_3$. The applied positive potential provides further driving force for the electrons to transfer through WO$_3$ NNs to FTO substrate, and then to the Pt counter electrode where they reduce water. The single crystalline structure of WO$_3$ NNs promotes the above-mentioned charge separation by greatly reducing the electron–hole recombination during charge transport. Moreover,

the needle-like nanostructure of photoanode provides large surface area for holes to react with water. These two factors benefit the photo-to-current efficiency. The Co-Pi layer, which acts as an OER catalyst, can efficiently capture photogenerated holes at the photoanode/solution interface and generates Co(IV) species [42], which are highly active toward water oxidation. The cobalt-based catalytic mechanism is also presented in Fig. 7. The Co(II) species can accept photogenerated holes from the valence band of Fe_2O_3 and then are oxidized to Co(III) species, which can be further oxidized to Co(IV) species due to the continuous hole injection from Fe_2O_3 to Co-Pi layer. The resulting Co(IV) species are highly active and can efficiently oxidize water to generate O_2 [42]. After reaction with water, the cobalt species return to their original valence state [40–43]. Therefore, the presence of Co-Pi facilitates the hole transfer from semiconductor oxides to water, and improves the stability of the composite photoanode by suppressing the photocorrosion that is induced by the hole accumulation at photoanode/solution interfaces.

4. Conclusions

The WO_3 NNs/Fe_2O_3 composite photoanodes have been successfully prepared on FTO substrates, with the high-aspect-ratio single crystalline WO_3 NNs as framework cores and small nanocrystals of α-Fe_2O_3 as porous shells. The modification of the WO_3 NNs with α-Fe_2O_3 greatly extends the light absorption band by redshifting the onset absorption wavelength from 450 nm to 650 nm. The composite photoanodes with a Fe_2O_3 growth time of 5 h exhibit the highest photocurrent, which is 1.6 times higher than that obtained on pure WO_3 NNs photoanode. The deposition of Co-Pi on the surface of WO_3 NNs/Fe_2O_3 composite significantly improves the photostability of the photoanodes by facilitating hole transfer from semiconductor oxides to water. The fabrication of the WO_3 NNs/Fe_2O_3/Co-Pi composite photoanodes is an efficient method to improve the OER performance of WO_3-based PEC cells. The present results also demonstrate that developing novel-structured photoelectrodes, which combine the merits of different compositions, i.e. good absorption properties of light harvesting materials, well-matched charge separation structures, and highly active OER or HER catalysts, offers promising opportunities for improving PEC water-splitting devices.

Acknowledgments

Appendix A. Supplementary data

Supplementary material related to this article can be found, in the online version, at http://dx.doi.org/10.1016/j.apcatb.2013.10.052.

References

[1] N.S. Lewis, D.G. Nocera, Proc. Natl. Acad. Sci. U.S.A. 103 (2006) 15729.
[2] M.G. Walter, E.L. Warren, J.R. McKone, S.W. Boettcher, Q. Mi, E.A. Santori, N.S. Lewis, Chem. Rev. 110 (2010) 6446.
[3] A. Fujishima, K. Honda, Nature 238 (1972) 37.
[4] J.K. Hurst, Science 328 (2010) 315.
[5] M. Gratzel, Nature 414 (2001) 338.
[6] D.C.a.J.M.G. Hodes, Nature 260 (1976) 312.
[7] C. Santato, M. Odziemkowski, M. Ulmann, J. Augustynski, J. Am. Chem. Soc. 123 (2001) 10639.
[8] C. Santato, M. Ulmann, J. Augustynski, Adv. Mater. 13 (2001) 511.
[9] J. Su, X. Feng, J.D. Sloppy, L. Guo, C.A. Grimes, Nano Lett. 11 (2010) 203.
[10] G. Wang, Y. Ling, H. Wang, X. Yang, C. Wang, J.Z. Zhang, Y. Li, Energy Environ. Sci. 5 (2012) 6180.
[11] D.-D. Qin, C.-L. Tao, S.A. Friesen, T.-H. Wang, O.K. Varghese, N.-Z. Bao, Z.-Y. Yang, T.E. Mallouk, C.A. Grimes, Chem. Commun. 48 (2012) 729.
[12] H. Ishihara, G.K. Kannarpady, K.R. Khedir, J. Woo, S. Trigwell, A.S. Biris, Phys. Chem. Chem. Phys. 13 (2011) 19553.
[13] J.C. Hill, K.-S. Choi, J. Phys. Chem. C 116 (2012) 7612.
[14] J.A. Seabold, K.-S. Choi, Chem. Mater. 23 (2011) 1105.
[15] Z. Jiao, J. Wang, L. Ke, X.W. Sun, H.V. Demir, ACS Appl. Mater. Interfaces 3 (2011) 229.
[16] J. Lin, P. Hu, Y. Zhang, M. Fan, Z. He, C.K. Ngaw, J.S.C. Loo, D. Liao, T.T.Y. Tan, RSC Adv. 3 (2013) 9330.
[17] D.W. Bullett, J. Phys. C: Solid State Phys. 16 (1983) 2197.
[18] S.K. Deb, Philos. Mag. 27 (1973) 801.
[19] M.A. Butler, J. Appl. Phys. 48 (1977) 1914.
[20] K. Sivula, F.L. Formal, M. Grätzel, Chem. Mater. 21 (2009) 2862.
[21] J. Su, L. Guo, N. Bao, C.A. Grimes, Nano Lett. 11 (2011) 1928.
[22] S.J. Hong, S. Lee, J.S. Jang, J.S. Lee, Energy Environ. Sci. 4 (2011) 1781.
[23] P. Chatchai, S.-y. Kishioka, Y. Murakami, A.Y. Nosaka, Y. Nosaka, Electrochim. Acta 55 (2010) 592.
[24] R. Solarska, R. Jurczakowski, J. Augustynski, Nanoscale 4 (2012) 1553.
[25] S.J. Hong, H. Jun, P.H. Borse, J.S. Lee, Int. J. Hydrogen Energy 34 (2009) 3234.
[26] R. Liu, Y. Lin, L.-Y. Chou, S.W. Sheehan, W. He, F. Zhang, H.J.M. Hou, D. Wang, Angew. Chem. Int. Ed. 50 (2011) 499.
[27] M.W. Kanan, D.G. Nocera, Science 321 (2008) 1072.
[28] N. Yoon-Chae, P. Indhumati, H. Robert, K.S. Nabeen, S. Patrik, Nanotechnology 21 (2010) 105704.
[29] L. Xi, P.D. Tran, S.Y. Chiam, P.S. Bassi, W.F. Mak, H.K. Mulmudi, S.K. Batabyal, J. Barber, J.S.C. Loo, L.H. Wong, J. Phys. Chem. C 116 (2012) 13884.
[30] D.K. Zhong, M. Cornuz, K. Sivula, M. Gratzel, D.R. Gamelin, Energy Environ. Sci. 4 (2011) 1759.
[31] E.M.P. Steinmiller, K.-S. Choi, Proc. Natl. Acad. Sci. U.S.A. 106 (2009) 20633.
[32] Y. Hou, F. Zuo, A. Dagg, P. Feng, Nano Lett. 12 (2012) 6464.
[33] S.K. Mohapatra, S.E. John, S. Banerjee, M. Misra, Chem. Mater. 21 (2009) 3048.
[34] F. Meng, S.A. Morin, S. Jin, J. Am. Chem. Soc. 133 (2011) 8408.
[35] B. Parkinson, Acc. Chem. Res. 17 (1984) 431.
[36] Z. Chen, T.F. Jaramillo, T.G. Deutsch, A. Kleiman-Shwarsctein, A.J. Forman, N. Gaillard, R. Garland, K. Takanabe, C. Heske, M. Sunkara, E.W. McFarland, K. Domen, E.L. Miller, J.A. Turner, H.N. Dinh, J. Mater. Res. 25 (2010) 3.
[37] X. Yang, A. Wolcott, G. Wang, A. Sobo, R.C. Fitzmorris, F. Qian, J.Z. Zhang, Y. Li, Nano Lett. 9 (2009) 2331.
[38] Y.-F. Lin, Y.-J. Hsu, Appl. Catal. B: Environ. 130–131 (2013) 93.
[39] D.K. Zhong, J. Sun, H. Inumaru, D.R. Gamelin, J. Am. Chem. Soc. 131 (2009) 6086.
[40] D.K. Zhong, D.R. Gamelin, J. Am. Chem. Soc. 132 (2010) 4202.
[41] D.K. Zhong, S. Choi, D.R. Gamelin, J. Am. Chem. Soc. 133 (2011) 18370.
[42] J.G. McAlpin, Y. Surendranath, M. Dincă, T.A. Stich, S.A. Stoian, W.H. Casey, D.G. Nocera, R.D. Britt, J. Am. Chem. Soc. 132 (2010) 6882.
[43] Y. Surendranath, M.W. Kanan, D.G. Nocera, J. Am. Chem. Soc. 132 (2010) 16501.